Marine and Petroleum Geology 165 (2024) 106875

Contents lists available at ScienceDirect

Marine and Petroleum Geology

journal homepage: www.elsevier.com/locate/marpetgeo

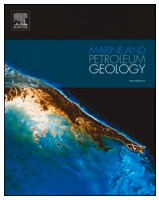

Formation of non-evaporitic gypsum in gas hydrate-bearing sediments at Håkon Mosby mud volcano, SW Barents sea

Cathrin Wittig [a,b], Claudio Argentino [c,*], Giuliana Panieri [c]

[a] Faculty of Sciences, Marine Biology Research Group, Ghent University, Ghent, Belgium
[b] Operational Directorate Natural Environment, Royal Belgian Institute of Natural Sciences, Brussels, Belgium
[c] Department of Geosciences, UiT – The Arctic University of Norway, Tromsø, Norway

ARTICLE INFO

Keywords:
Methane seep
Håkon Mosby mud volcano
Anaerobic oxidation of methane
Barite
Gypsum
Authigenic carbonate

ABSTRACT

Authigenic minerals such as carbonate and iron sulfide are known features at cold seeps worldwide and form as a result of the anaerobic oxidation of methane in the sulfate-methane transition zone (SMTZ). Recent findings of seep-related non-evaporitic gypsum raise questions regarding its distribution, formation mechanisms, and relationships with the other proxies for confident paleo-seep reconstructions. Here, we report new findings of gypsum in the seep-impacted sediments of the hydrate-bearing Håkon Mosby mud volcano, SW Barents Sea. We combined sediment core logging (XRF, X-Ray) with optical microscopy and scanning electron microscopy - electron dispersive energy to characterize the authigenic mineral fraction of the sediment. Three paleo-SMTZs marked by the co-occurrence of pyrite and gypsum accumulations were found at 7–10 cm, 13–18 cm and 19–21 cm, above the modern one (at ~50 cm) and match with carbonate-poor and foraminifera-free sediment intervals. Our results indicate that gypsum formation required a descending SMTZ (decreasing methane flux), triggering the oxidation of previously-formed pyrite which supplied extra SO_4^{2-} to the pore water. Acidic conditions caused by pyrite oxidation would have promoted the dissolution of carbonate particles, thus releasing Ca^{2+} that is available for gypsum formation. As seen in other studies, the presence of shallow gas hydrates seems to play an important role as a calcium source for gypsum precipitation, via ion exclusion during hydrate formation. HMMV represents an optimal natural laboratory to investigate the interplay between different processes in gypsum biogeochemistry and its potential use as a proxy for methane seeps in modern and ancient settings.

1. Introduction

Authigenic minerals in methane seepage environments such as carbonate, barite and iron sulfides have been reported from cold seeps worldwide, e.g. the Gulf of Cadiz, the eastern Mediterranean Sea, the Black Sea) (Foucher et al., 2009; Suess, 2020; Bohrmann and Torres, 2016). Recently, non-evaporitic gypsum associated with cold seep activity has also been reported in the South China Sea (Lin et al., 2016; Zhao et al., 2021), the SW African margin (Pierre, 2017), and in Arctic regions (Argentino et al., 2021; Himmler et al., 2019; Panieri et al., 2017).

The formation of authigenic minerals in cold seep environments is commonly associated with the process of sulfate-driven anaerobic oxidation of methane (AOM) performed by a consortium of methane-oxidizing archaea and sulfate-reducing bacteria generating an increase in bicarbonate and hydrogen sulfide in the pore waters (Boetius and Wenzhöfer, 2013). AOM is considered the most critical process in cold seep environments as it consumes up to 90 % of the ascending methane (Reeburgh, 2007) and influences the redox conditions in the sediment as well as the distribution of chemosynthetic communities at the seafloor (Argentino et al., 2022; Foucher et al., 2009; Jerosch et al., 2007).The highest rate of AOM is found in the sediment interval at the interception between the sulfate and methane concentration profiles, known as the Sulfate-Methane-Transition Zone (SMTZ) (Ruban et al., 2020; Wallmann and Schicks, 2020; Whiticar and Faber, 1986, Whiticar, 2020).

Methane-derived authigenic carbonates (MDAC), occurring as massive crusts on the seafloor or nodules (mm to cm in size) in the sediment, are formed because of an intense AOM, which increases the pore water alkalinity through enhanced production of dissolved inorganic carbon (bicarbonate HCO_3^-). When combined with a sufficient amount of seawater cations (Ca^{2+}; Mg^{2+}), the formation of carbonate and in-situ precipitation is promoted (Argentino et al., 2021; Himmler

* Corresponding author.
E-mail address: claudio.argentino@uit.no (C. Argentino).

https://doi.org/10.1016/j.marpetgeo.2024.106875
Received 29 November 2023; Received in revised form 3 April 2024; Accepted 25 April 2024
Available online 29 April 2024

et al., 2019; Kravchishina et al., 2021; Ruban et al., 2020; Yao et al., 2020).

Hydrogen sulfide released by AOM in the SMTZ combines with reactive iron to generate pyrite (FeS_2) over a metastable intermediate stage of iron monosulfides (mackinawite (FeS); greigite (Fe_3S_4)) (Bazzaro et al., 2020; Jørgensen, 2021; Ruban et al., 2020; Schippers and Jorgensen, 2002). This process eventually leads to the accumulation of pyrite in the SMTZ. Authigenic pyrite at seep sites often occurs in framboids of several μm in the sediment (Kravchishina et al., 2021; Milkov et al., 2004), forming enrichments detectable as magnetic susceptibility drops (Johnson et al., 2021) and/or low total organic carbon/total sulfur ratios (Argentino et al., 2021).

Diagenetic barite accumulations ("barite fronts") in the shallow sediments of a cold seep area form when upward diffusing barium meets downward diffusing sulfate from the bottom waters (Riedinger et al., 2006). In the sulfate-depleted areas below the SMTZ, barite dissolves back into the pore water and consequentially rises upwards into the sulfate-rich pore water to ensure an equilibrium state (Carter et al., 2020). Therefore, barite accumulates at the top of the SMTZ where enough sulfate and barium lead to pore water oversaturation of barite, and a stable or descending SMTZ favors its preservation (Argentino et al., 2021, 2023; Riedinger et al., 2006; Vanneste et al., 2013; Yao et al., 2020).

These authigenic minerals create a distinctive footprint in the sedimentary record and are used to track the vertical shifts of the SMTZ linked to changes in methane fluxes (Argentino et al., 2021; Chen et al., 2023; Hu et al., 2020; Suess, 2020; Bohrmann and Torres, 2016; Yao et al., 2020). Furthermore, their stable isotopic composition and formation processes can give essential implications for the cycling of key biogeochemical elements (Ca, Ba, Fe, S) at cold seeps (Gong et al., 2023; Lin et al., 2016; Riedinger et al., 2006; Ruban et al., 2020; Zhao et al., 2021).

Non-evaporitic gypsum at cold seeps has only been reported from a few locations worldwide, e.g. from the South and the East China Sea (Lin et al., 2016; Liu et al., 2018; Zhou et al., 2020; Zhao et al., 2021; Sun et al., 2023), South Atlantic (Dantas et al., 2022), offshore Eastern India (Kocherla, 2013), southwest African Margin (Pierre, 2017) and Gulf of Cadiz (Pirlet et al., 2012). Those studies utilized different approaches to determine the origin of gypsum, based on microscopy (Pirlet et al., 2012; Kocherla, 2013; Zhou et al., 2020; Sun et al., 2023) and stable isotope composition ($\delta^{34}S$ and $\delta^{18}O$)(Lin et al., 2016; Liu et al., 2018; Pierre, 2017; Zhang et al., 2018; Zhao et al., 2021; Dantas et al., 2022). The most common gypsum morphologies in seep-impacted sediments include euhedral rhombic and trapezoidal shapes, acicular microcrystals and prismatic rosettes, occasionally aggregated in clusters. Gypsum generally co-occurs with pyrite at paleo-SMTZs and shows isotopically-depleted $\delta^{34}S$ and $\delta^{18}O$ values compared to seawater (Pierre, 2017; Liu et al., 2018; Zhang et al., 2018), indicating a contribution from pyrite re-oxidation during phases of descending SMTZs. In most cases, the gypsum is associated with shallow gas hydrates, thus leading some authors to propose ion exclusion during hydrate formation as an additional source of dissolved Ca^{2+} for gypsum (Lin et al., 2016; Zhang et al., 2018). The factors controlling gypsum stratigraphic distribution, formation mechanisms, and the relationships with gas hydrates remain poorly understood. Unraveling the dynamics of gypsum authigenesis at gas-hydrate bearing settings will be critical for its confident use as a proxy for methane emissions in modern and paleo records.

This study intends to investigate non-evaporitic gypsum found in the shallow sediments of the hydrate-bearing Håkon Mosby mud volcano (HMMV), SW Barents Sea, as well as its genetic and stratigraphic relationships with other observed authigenic minerals. Findings of gypsum in the sand fraction of shallow sediments at the HMMV have been previously reported (Milkov et al., 2004), but never investigated in detail regarding their distribution, morphology and possible formation mechanisms. Here, this is achieved by applying geochemical, microscopic, and spectroscopic analyses on a seep-impacted gravity core recovered from the HMMV on the research cruise CAGE-20-3 onboard the R/V Helmer Hanssen.

2. Study area

The HMMV (72°00.3′N, 14°44.0′E) is located at a water depth of 1250–1260 m along the western margin of the SW Barents Sea (Fig. 1a). The HMMV is characterized by a flat dome-like circular shape with a width of 1.4 km, an area of 1.2 km^2 and a maximum height of 16 m (Foucher et al., 2010; Milkov et al., 2004; Pape et al., 2011; Perez-Garcia et al., 2009; Vogt et al., 1997) (Fig. 1b and c). Its morphology is dominated by its circular low relief structure, only limited by surrounding subsidence faults, and is built by mud-flows and uplift events resulting from active eruptions of the mud volcano.

The formation of the HMMV is mainly attributed to glacial sediment overloading and resulting overpressure in underlying organic rich sediments. These sediments are defined as preglacial biosiliceous oozes that were deposited in the early-mid Cenozoic (>2.3 Ma) (in several preglacial Eocene, Oligocene, Early-Middle Miocene and Late Miocene-Pliocene sequences) and represent the main hydrocarbon reservoir of the HMMV (Berndt et al., 2006; Hjelstuen et al., 1999; Perez-Garcia et al., 2009).

Since the discovery of the HMMV in 1989 on a geophysical mapping survey, several studies were conducted in the area. Side-scan, shallow acoustic and remotely-operated vehicle (ROV) surveys revealed gas hydrate accumulations in the shallow surrounding sediments, gas flares in the water column and a distinctive distribution of chemosynthetic communities (e.g. tube worms and microbial mats) (Fallati et al., 2023, Fallati and Panieri, 2023; Milkov et al., 2004; Niemann et al., 2006; Pape et al., 2011). Various cores and sediment samples were collected and microbial activity and AOM were confirmed through isotopic evidence and pore water profiles (Milkov et al., 2004; Niemann et al., 2006; Pape et al., 2011). High geothermal gradients of 20–40 °C/m were confirmed through in-situ temperature measurements in the shallow sediments and active mud flows were observed as well (Fallati et al., 2023, Feseker et al., 2008, 2014; Foucher et al., 2010; Lösekann et al., 2007; Milkov et al., 2004; Niemann et al., 2006; Vogt et al., 1997). Based on these previous studies and observations, the HMMV is considered an active Arctic deep-sea mud volcano associated with intense AOM in the subsurface.

3. Materials and methods

Two gravity cores, CAGE20-3-HH-367-GC and CAGE20-3-HH-369-GC, hereafter named 367-GC and 369-GC, respectively, were recovered in 2020 during the research cruise CAGE-20-3 onboard the R/V Helmer Hanssen (Waghorn et al., 2020). 367-GC was collected within the mud volcano and included gas hydrate layers that readily dissolved onboard upon recovery. A previous study by Argentino et al. (2023) identified a shallow modern SMTZ at around 50 cm, and based on organic carbon and nitrogen geochemistry the authors found two paleo-SMTZs at 14–16 cm and below 55 cm. The top of the gas hydrate layer was stratigraphically located at 67 cm in 367-GC. Therefore, this core is the primary focus of this study on authigenic phases. 369-GC was collected 16 km away from the HMMV in a non-seepage area, so it is used as a reference core. After the recovery, the cores were cut into 1 m sections, sampled for pore waters and safely stored in a cooling room at 4 °C until further treatment in the laboratory onshore. The pore water data (SO_4^{2-}, DIC) reported in the figures (Figs. 2 and 3) are after Argentino et al. (2023), and included in our study to show the position of the modern SMTZ.

3.1. Core logging: X-ray imaging and X-ray fluorescence (XRF)

Before opening the cores for sub-sampling, non-destructive X-Ray

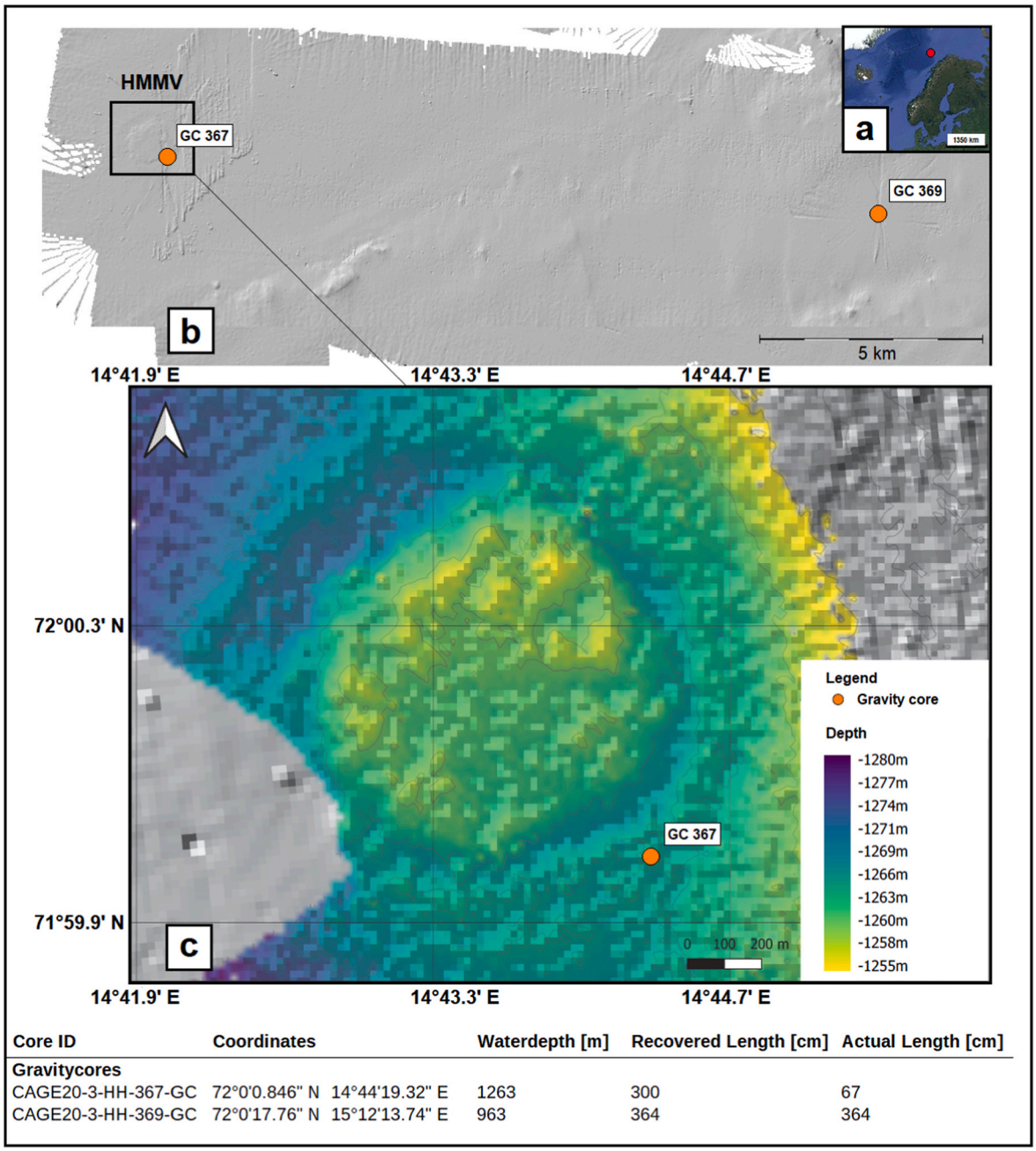

Core ID	Coordinates	Waterdepth [m]	Recovered Length [cm]	Actual Length [cm]
Gravitycores				
CAGE20-3-HH-367-GC	72°0'0.846" N 14°44'19.32" E	1263	300	67
CAGE20-3-HH-369-GC	72°0'17.76" N 15°12'13.74" E	963	364	364

Fig. 1. Location of the HMMV on the SW Barents Sea slope (a) and of the two gravity cores (orange) discussed in this study (b). C) Microbathymetry of the HMMV acquired during the AKMA 2021 Expedition (Bünz and Panieri, 2022) showing the location of core 367-GC on the rim of the mud volcano and the reference core 369-GC ~16 km away from the mud volcano.

imaging and X-Ray fluorescence analyses were performed at the Department of Geosciences, UiT- The Arctic University of Norway, Tromsø (Norway). High-resolution (30 μm–150 μm) 2D-X-Ray radiographs of the whole cores obtained with a Geotek X-Ray CT system revealed the sedimentological structures. The data was collected through plastic liners with an X-ray voltage of 130 V and a frame rate of 30 frames per second, respectively. The data files were exported as grey-scale tiff images. The contrast values of these images were manipulated through the Geotek X-ray viewer software afterwards to highlight specific features. XRF data was acquired with the Avaatech XRF core scanner to obtain information on downcore variations in the elemental composition and content of the sediment. XRF datasets were obtained in several runs depending on the energy needed to measure a specific elemental range. Specific filters were also included in each run to exclude the influence of lighter elements when measuring heavier ones. For this study three runs with a resolution of 1 cm: 10 kV, 1 mA, no filter; 30 kV, 2 mA, Pd-thick filter; 50 kV, 2 mA, Cu-filter. In addition to the qualitative and quantitative element composition of the material, detailed photographs with a high resolution were taken by a digital Color Line Scan Camera. The data was processed and plotted as elemental ratios using Ti for matrix-effect correction and transformed to natural logarithm. We focused on ln(S/Ti), ln(Fe/Ti), ln(Ba/Ti) and ln (Ca/Ti) profiles to discuss the origin of authigenic phases in relation to SMTZs. X-Ray radiographs and ln(Ba/Ti) and ln(Ca/Ti) profiles were presented in Argentino et al. (2023) whereas ln(S/Ti), ln(Fe/Ti) are discussed here for the first time.

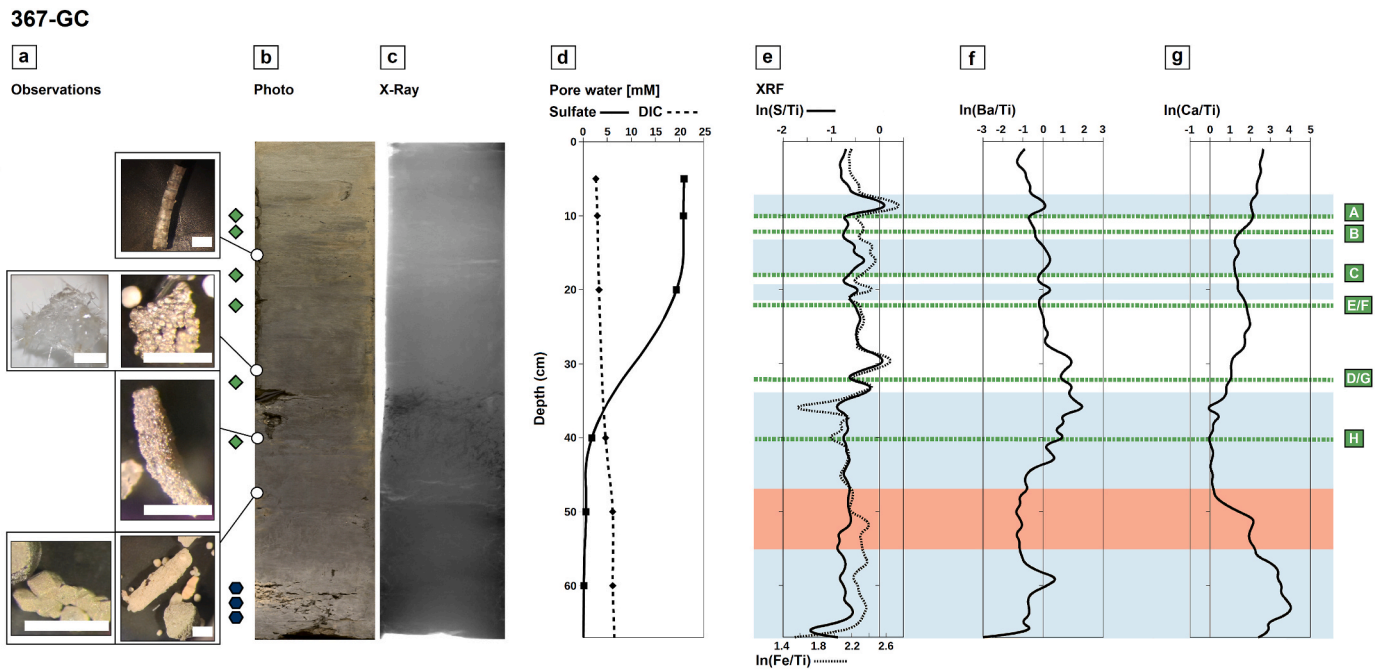

Fig. 2. Microscope observations, pore water chemistry and XRF data of 367-GC. Microscope observations of pyrite tubes and framboids and sponge spiculae from different sediment layers (a) (scale bar is 2 mm); photograph (b) and X-Ray image (c) of the core; sulfate and DIC pore water concentration profiles (d); XRF profiles of ln(S/Ti) and ln(Fe/Ti) (e), ln(Ba/Ti) (f) and ln(Ca/Ti) (g). The findings of gypsum (green diamond and green dotted line) and carbonate nodules (blue hexagon) in the microscopic analysis are reported next to the core photo. Pore water and XRF Ca, Ba data after Argentino et al. (2023). The letters on the right (green boxes) refer to crystals isolated for SEM-EDS analyses. Anomalies associated with the modern SMTZ identified from the pore waters and Ba and Ca counts of the XRF data are shown in red, while others associated with a paleo SMTZ are shown in light blue.

3.2. Sampling procedure and microscope analysis

The cores were split into halves, and described in terms of sediment texture and main lithology as well as colour gradients after the Munsell soil colour chart. Core 367-GC was sampled every cm for geochemical investigations (carbon-nitrogen systematics) presented in Argentino et al. (2023) until 67 cm below the seafloor (bsf), depth of the top of the hydrate layer. Aliquots of dry sediment were prepared for microscopic investigations. After freeze-drying, the samples for this study were wet sieved at >125 μm using sieves and filterpaper, dried in the oven (40 °C), weighed, and labelled accordingly. The dry fraction of >125 μm was examined in detail under an optical microscope at the Department of Geosciences (UiT). Based on the petrographic screening of microcrystals found in the samples, we picked specimens suspected to be barite and gypsum for further investigation with Scanning Electron Microscopy and Energy Dispersive X-ray Spectroscopy (SEM- EDS). The specimens were carbon-coated to enhance the conductivity and then analyzed with a SEM Hitachi Tabletop Microscope TM-3000 at the Department of Geosciences (UiT).

4. Results

4.1. Sedimentology

The gas hydrate-bearing core 367-GC shows a homogeneous non-layered sedimentation character, dominated by silty clay and with signs of heavy bioturbation until around 38 cm bsf. Lighter silty clay (2.5Y 5/3 light olive brown) (~0–12 cm bsf) is visible at the top before the sediment becomes more compacted and darker (2.5Y 4/2 olive brown) (12–50 cm) downcore. A layer characterized by hard concretions (33–46 cm bsf) was identified in the X-Ray and by visual observation of white patches by Argentino et al. (2023). We found that this layer hosts widespread spiculae of sponges (Fig. 2a). The downmost sediment is of brownish-grey color (2.5Y 5/1 Gy to 2.5Y 6/2 light brownish grey) and exhibits a compact character (dark X-Ray signals) (Fig. 2a and b). The reference core 369-GC exhibits continuous sedimentation with a modern bioturbated oxidized horizon out of sandy mud (0–5 cm bsf) at the top (10 YR 5/6 yellowish brown) and brown interlayered mud (2.5Y 4/2 dark greyish brown) downcore, which is only interrupted by a layer of dark homogeneous clay (2.5Y 3/1 very dark grey) with coarser grains (132–268 cm bsf)(Fig. 3a and b).

4.2. XRF

The down-core elemental variations of S, Fe, Ba and Ca, here plotted as log-elemental ratios, showed different trends in the two investigated cores. In core 369-GC, ln(S/Ti) varies between −3 and −1.5 with rather stable trends down to 270 cm bsf followed by a localized drop and lower values in the lower part of the core (Fig. 3d). This pattern is associated with a change in color and composition visible in the photographs (Fig. 3a) and X-Ray radiograph (Fig. 2b). The ln(Fe/Ti) profile does not vary much, with values fluctuating around −1 (Fig. 3d). There are some positive peaks between 0 and 10 cm 90–100 cm, at 140 cm, 160 cm and 270 cm. Some of those peaks correspond to positive excursions in ln(S/Ti) values (e.g. 90–100 cm), whereas others correspond to drops in ln(S/Ti) values (e.g. 0–10 cm). The ln(Ba/Ti) profile shows values between −1.5 and −1 (Fig. 3e) and an overall similar trend to ln(S/Ti). Calcium displays large variations corresponding to three well-defined intervals 0–140 cm, 140–270 cm and 270–360 cm (Fig. 3f).

Core 367-GC displays large variations compared to 369-GC in all the XRF profiles (Fig. 2). Ln(Fe/Ti) and ln(S/Ti) profiles show a tight positive correlation, with the main positive peaks identified in the intervals 7–10 cm, 13–18 cm, 19–21 cm, 29–31 cm, 32–34 cm and 50–52 cm bsf (Fig. 2d). The highest ln(Ba/Ti) values are located in an interval 29–44 cm bsf and correspond to multiple peaks with the highest values found at 35–37 cm bsf. Other smaller isolated enrichments are found at 7–10 cm; 13–18 cm; 19–21 cm and 58–60 cm bsf (Fig. 2e). Ln(Ca/Ti) values decrease from the surface down to 40 cm and then rise again until

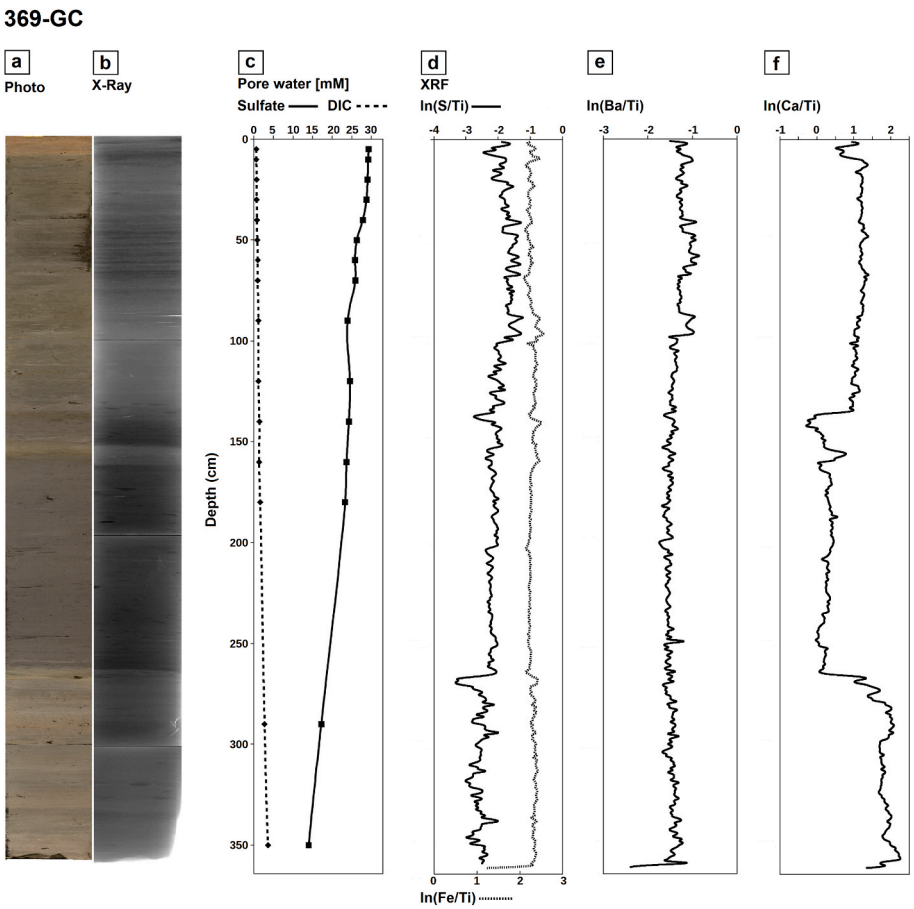

Fig. 3. Results of 369-GC (reference core). The photography, the X-Ray image, pore water and XRF datasets (S, Fe, Ba and Ca) are displayed from left to right (a–f). Evidence for seep activity was not reported, and no gypsum crystals or carbonate nodules were found. Pore water and XRF Ca, Ba data after Argentino et al. (2023).

reaching a maximum at 62–64 cm bsf (Fig. 2f). Elevated ln(Ca/Ti) values are found in the interval 50–67 cm bsf, which matches with the occurrence of microscopic carbonate concretions as reported in Argentino et al. (2023).

4.3. Microscopic observations and SEM/EDS analysis

Optical microscopy investigations on 367-GC revealed high amounts of pyrite in specific intervals, occurring as pyritized tubes and microcrystal aggregates. The highest number of observations (~50 particles per dry gram) were found in the interval 36–48 cm bsf, while smaller accumulations of pyrite (~30 particles per dry gram) were observed in 8 and 20 cm bsf. These intervals roughly match the ln(S/Ti) and ln(Fe/Ti) peaks in Fig. 2e. Pyrite tubes were found from the surface layer down to 38 cm (Fig. 2a). Carbonate micro-concretions and foraminifera overgrowth were observed at 10–20 cm bsf and larger amounts of carbonates were present at 60–61 cm, 62–63 cm and 64–65 cm bsf. Although foraminifera were not further investigated in this study, it is worth mentioning that foraminifera were not present in the interval from ~38 to 48 cm bsf. Unusually high amounts of sponge spiculae were present from the surface down to 38 cm bsf. Several prominent gypsum crystals of the size of ~1–2.5 mm were found at 10–11 cm, 12–13 cm, 18–19 cm, 22–23 cm, 32–33 cm, 40–41 cm bsf in the coarse fraction (≥125 μm) of 367-GC and further investigated with the SEM/EDS. Most of the crystals are well preserved with a transparent character and show colors from white to yellow/brownish. The EDS reveals a dominant composition of the elements S and Ca in an approximate relation of 1:1 or at least 1:0.8 for all of the crystals. Furthermore, these crystals display various habits, as well as singular and multiple crystal structures. Three main different crystal habits were identified, and they represent the faces of the known crystal system of gypsum in different scales (monoclinic system, prismatic class). Type 1 shows a prominent pinacoid face with an elongated hexagon shape with a fibrous surface as well as a sheeted step-like structure (e.g. Crystal A in Fig. 2)(Fig. 4a). Type 2 shows a an elongated prismatic crystal habit with dominant prismatic faces as well as smooth surface ony interrupted by parallel growth lines (e.g. Crystals B and C in Fig. 2)(Fig. 4b and c). Type 3A shows several types of crystals intertwined with each other largely associated with 3B and occasionally Type 2 (e.g. Crystals D, E and F in Fig. 2) (Fig. 4d, e, f). Type 3B shows a prominent pinacoid face with a parallelogram shape and a smoother surface interrupted by sheeted step-like structures (e.g. Crystals G and H in Fig. 2)(Fig. 4g and h). Silicate fragments with higher amounts of Si, Al and K were observed on several crystals of different types (Fig. 4b, c, d, e, h).

5. Discussion

5.1. Methane dynamics recorded by authigenic minerals

The stratigraphic distribution of geochemical anomalies of S, Fe, Ca and Ba obtained from the XRF analysis was used to detect the enrichments in authigenic minerals produced by AOM. When methane oxidation is coupled to sulfate reduction, the co-precipitation of authigenic carbonate (aragonite or Mg-calcite) and iron sulfides (pyrite) is induced at the SMTZ. The presence of those phases in narrow sediment intervals is reflected by high ln(Ca/Ti), ln(Fe/Ti) and ln(S/Ti) in the XRF profiles. Barium is a well-established proxy for barite fronts at cold seeps, generating narrow peaks at the top of the SMTZs, generally above

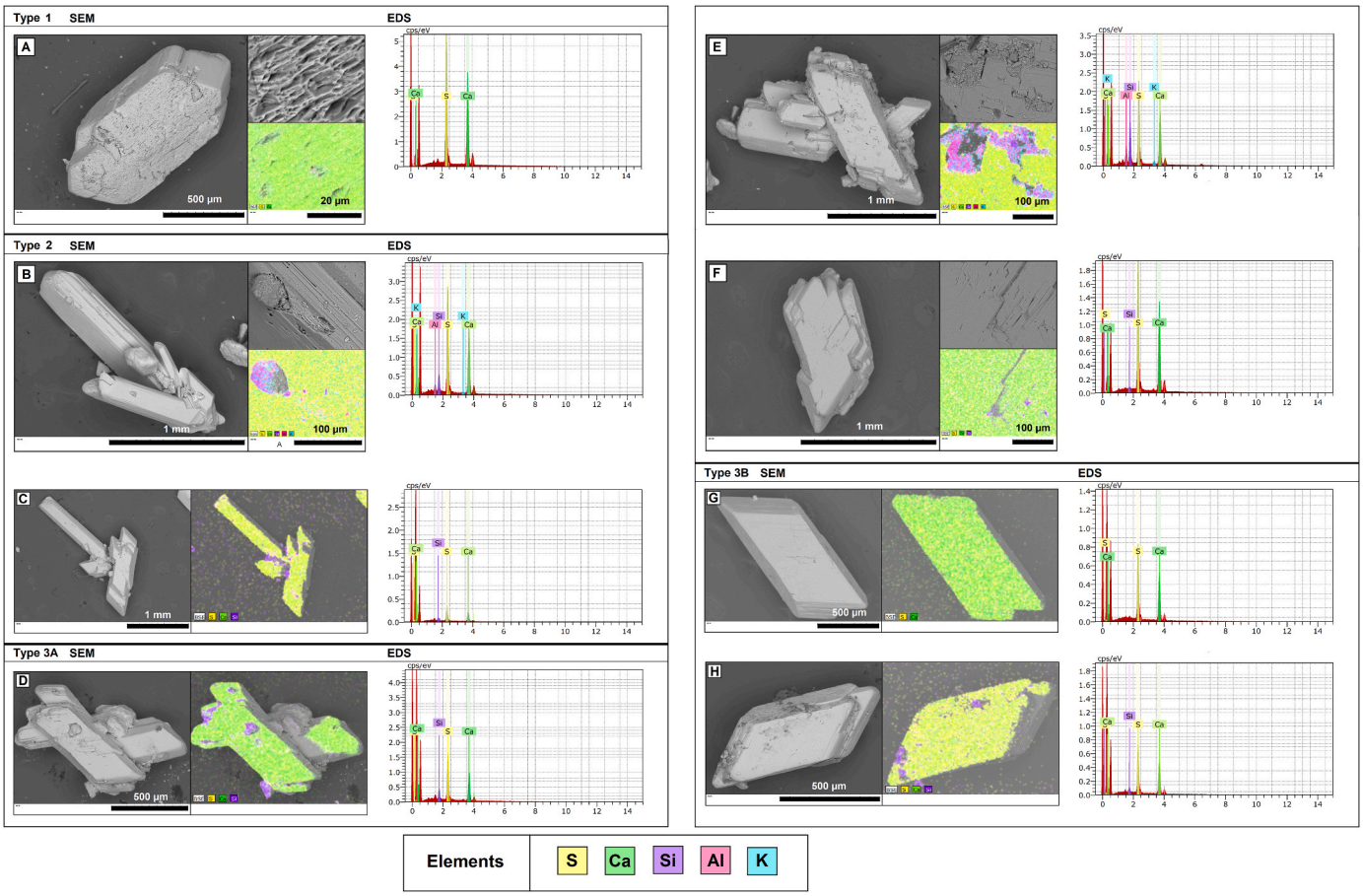

Fig. 4. SEM-EDS results of gypsum crystals isolated from dry sediment samples A-H (Fig. 2).Three main different crystal habits (Type 1–3) were identified and display dominant pinacoid and prismatic faces as well as an often fibrous character with a sheeted step-like structure. The EDS reveals an elemental composition dominated by S and Ca in a relation of 1:1 for all the crystals. Some aluminosilicates are found on the surface of some gypsum crystals.

or partially overlapping with the carbonate and pyrite enrichments (e.g. Argentino et al., 2021; Yao et al., 2020). Argentino et al. (2023) identified two paleo-SMTZ in core 367-GC (14-16 cm and below 50 cm) based on Ca and Ba distribution and ^{13}C-depleted organic carbon as negative as −42.0 ‰ related to methanotrophic biomass. The modern SMTZ was found at ~50 cm where pore water sulfate is fully consumed and dissolved inorganic carbon shows its lowest isotopic value of −31.2 ‰ consistent with the release of methane-derived carbon by AOM. Through our detailed microscopic investigations on dry sediment samples and the integration of XRF data of Fe and S which were not included in Argentino et al. (2023), we identified two new paleo-SMTZs.

Three paleo-SMTZs occur above the modern SMTZ at 7–10 cm, 13–18 cm (matching the one at 14-16 cm of Argentino et al., 2023) and 19–21 cm, based on the occurrence of enrichments in S and Fe (Fig. 2e) co-occurring with smaller peaks in Ba (Fig. 2f). In these narrow intervals we observed several pyrite and barite particles. A few carbonate micro-concretions and carbonate overgrowth on foraminifera shells were observed at 10–20 cm. The interval 13–18 cm, in particular, matches the uppermost paleo-SMTZ identified in the previous study, whereas the other two interval are reported here for the first time and highlight the complexity of paleo-SMTZ reconstructions relying on the type and number of proxies employed (Yao et al., 2020). The preservation of barite crystals in these three layers suggests a descending SMTZ pattern because the geochemical conditions, i.e. low SO_4^{2-}, below the SMTZ would have led to their dissolution (Carter et al., 2020). The sedimentation rates for the southwestern Barents Sea close to the study area are ~4–15 cm/kyr (Faust et al., 2020). These values were rather constant over the Holocene and late deglaciation (0–12 ka) and higher during the Last Glacial Maximum and early deglaciation (~12–24 ka) with values in the range 35–80 cm/kyr (Levitan and Lavrushin, 2009). According to these values, the uppermost paleo-SMTZ at 10 cm must have formed later than 2.5 ka (maximum age of the host sediment interval extrapolated using the lowest endmember of Holocene sedimentation rates). The base of Holocene deposits in the cores would be approximatively between 40 cm and 150 cm. The modern SMTZ is located at ~50 cm and associated with a prominent barite front at 29–44 cm (Fig. 2a–e). Then, another paleo-SMTZ below 50 cm is associated with authigenic carbonates (50–67 cm) with a typical methane-related isotopic signature ($\delta^{13}C = -31.8$; Argentino et al., 2023). Here, we found that this interval is also associated with large amounts of pyrite seen in microscopic observations (Fig. 2a) and highlighted by high ln(Fe/Ti) values (Fig. 2e). These geochemical anomalies point to long stable methane fluxes as enough time (centuries to thousands of years) for AOM is needed to form and preserve the observed prominent proxy signatures of carbonate and barite (Riedinger et al., 2006; Vanneste et al., 2013; Himmler et al., 2019; Kravchishina et al., 2021; Ruban et al., 2020). Moreover, this paleo-SMTZ is recorded in sediments older than 12.5 ka. The timing of formation of these geochemical anomalies and the estimated age of the uppermost paleo-SMTZ imply that this lowermost paleo-SMTZ must have preceded the other three. On the other hand, the concave-up sulfate pore water profile suggests transient conditions with an increasing flux in the last tens to hundreds of years likely modulated by the shallow hydrate layer (Argentino et al., 2023).

5.2. Authigenic origin of gypsum

The gypsum crystals discussed in this study are authigenically precipitated and related to the process of AOM in the shallow sediments of the HMMV. This is supported by the findings of gypsum in the intervals coinciding with the identified SMTZs, as well as the observed morphology of the crystals. Gypsum was found in several layers (10–11 cm, 12–13 cm, 18–19 cm, 22–23 cm, 32–33 cm, 40–41 cm) all located above the modern SMTZs. As these crystals display various habits (Type 1–3), singular and multiple crystal structures on average ~1 mm in size, an in-situ formation seems likely (Lin et al., 2016). The crystals also show no signs of alteration or abrasion on the surfaces and seem overall well preserved. Other studies discussing the morphology of gypsum crystals in a cold seep system also reported twinned and singular forms, as well as euhedral rhombic, trapezoidal, prismatic and rosette like habits (Dantas et al., 2022; Lin et al., 2016; Zhao et al., 2021), although the latter was not found in this study. These observed differences in the morphology of gypsum crystals are probably linked to the chemical pore water composition (SO_4^{2-} and Ca^{2+} concentration) controlling the precipitation rates (Lin et al., 2016). The predominant elongated crystals found in 367-GC would indicate fast growth rates under higher degrees of supersaturation.

The formation of gypsum can occur after retrieving the cores as a storing artifact caused by oxidation of sulfides or sample drying. Calculations from (Lin et al., 2016) after (Kopittke et al., 2004) regarding the sufficient amount of evaporated pore water needed to form large gypsum accumulations after core retrieval indicate that ~0.1 g of gypsum would require 29 mL of fully evaporated seawater. We did not quantify the amount of gypsum in the different specimens. As described in Argentino et al. (2023), the core containing the gypsum enrichments was rather dry and presents lower porosity close to the top of the hydrate layer, reflecting the absorption of water molecules during gas hydrate formation. Therefore, it is unlikely that the sediment samples contained enough water to induce the formation of large gypsum crystals. Moreover, the examined cores 367-GC and 369-GC were treated and stored under identical conditions, but only the gas hydrate-bearing core 367-GC host the gypsum enrichments, so we can rule out gypsum formation during storage.

5.3. Diagenetic model

To explain the distribution of gypsum crystals found in GC367 and their formation coupled to the dynamic methane flux environment of the HMMV (Fig. 5), we envisioned a series of diagenetic processes.

An initial constant active methane flow linked to the shallow gas hydrates induced the formation of the authigenic carbonates observed at 50–67 cm (paleo-SMTZ1) through a rise in alkalinity caused by protracted AOM. This stage occurred later than 12.5 ka. Carbonate precipitation was associated with pyrite formation. After centuries to a few thousands of years, the time needed to form such diagenetic enrichments, the methane flux from the hydrates increased and caused the SMTZ to migrate upward (paleo-SMTZ2). The AOM activity generated the anomalies recorded at 7–10 cm. At the time when the SMTZ was active, extensive amounts of pyrite were produced through a high AOM rate, and a small barite front was formed.

With time, the methane flux from the underlying hydrates progressively decreased, and the SMTZ deepened, forming the anomalies observed at 13–18 cm (paleo-SMTZ3) and at 19–21 cm(paleo-SMTZ4). With the downward migration of the SMTZ, barite fronts were preserved, whereas the pyrite produced in previous horizons became exposed to oxygenated conditions which led to its oxidation.After the descending phase of the SMTZ, the methane flux probably raised again and pushed the SMTZ to modern position. This is indicated by the concave-up shape of the sulfate concentration profile which is consistent with transient conditions with a recent increase in methane fluxes.

To form authigenic gypsum in-situ in a sedimentary environment

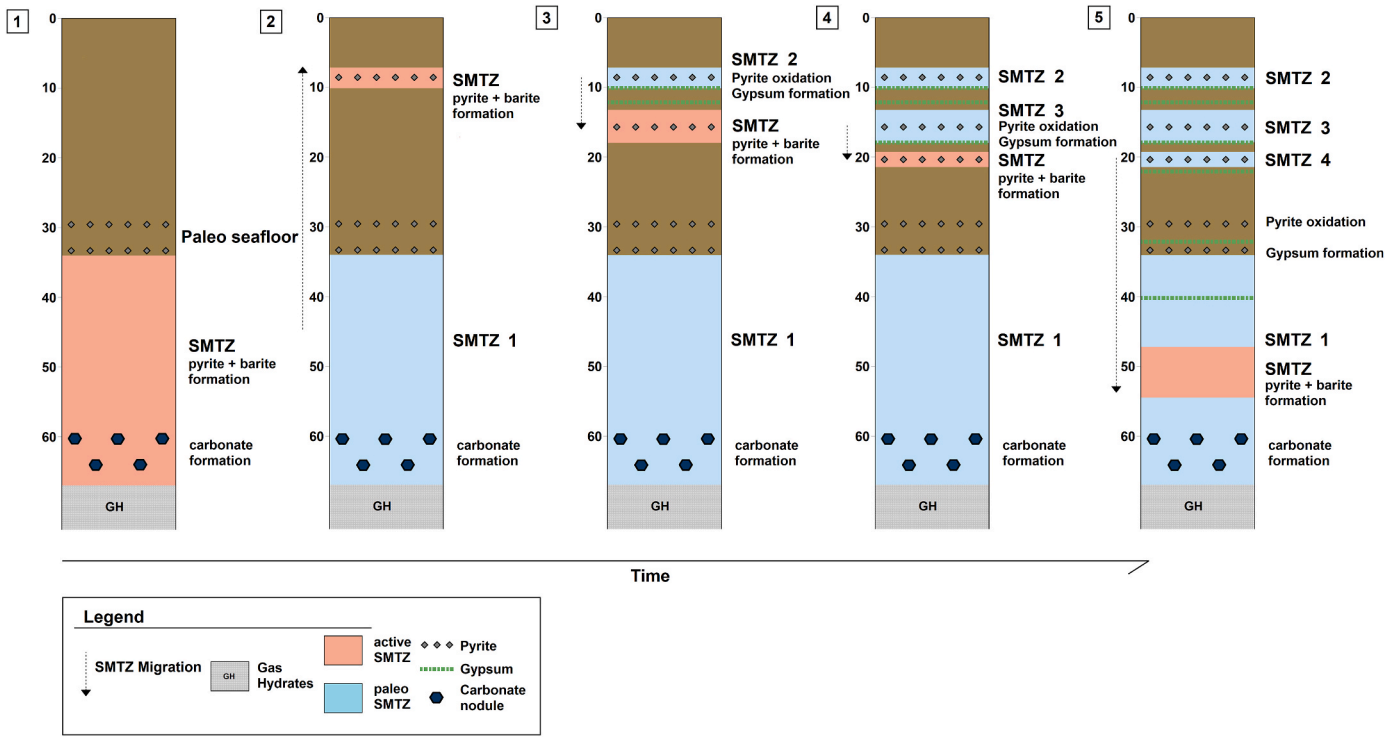

Fig. 5. Simplified diagenetic model of 367-GC. The formation of the observed distribution of gypsum (dotted green line) is shown in relation to the occurrence of other authigenic minerals (e.g. carbonate (blue hexagon) and pyrite (grey diamond) and the established methane emission history in 5 stages (from left to right). The direction of SMTZ migration is indicated by an arrow. The active SMTZ in each stage is shown in orange, while paleo-SMTZs are light blue. As discussed in the text, these events likely occurred later than 12.5 ka. The present-day SMTZ shows a concave-up sulfate profile, possibly indicating a relatively recent increase in methane flux not shown in the model.

after deposition, a sufficient amount of Ca^{2+} and SO_4^{2-} in the pore water is needed (Dantas et al., 2022; Hoareau et al., 2011; Lin et al., 2016). The main sources of sulfate for gypsum formation at cold seeps are seawater and sedimentary sulfide minerals (mostly from AOM)(Lin et al., 2016). Sulfate in a normal marine sedimentary environment is mostly derived from seawater (28 mM on average after (Hoareau et al., 2011)) diffusing from the bottom waters into the sediment. This sulfate becomes microbially consumed (reduced) in the process of organic matter degradation with increasing depth and forms iron sulfide minerals (e.g. pyrite) (Bazzaro et al., 2020; Hong et al., 2020). At cold seeps, the process of AOM additionally reduces sulfate to sulfide, which induces pyrite accumulation . The (re)oxidation of pyrite or other sulfide minerals when exposed to oxygenated conditions seems a prerequisite for gypsum formation (Dantas et al., 2022; Lin et al., 2016; Liu et al., 2018; Pierre, 2017; Zhang et al., 2018; Zhao et al., 2021). This process releases a significant amount of SO_4^{2-} back to the pore water that is necessary to reach gypsum supersaturation and inducing its precipitation in narrow sediment layers (Eq. (R1)).

$$FeS_2 + H_2O + \frac{7}{2}O_2 \rightarrow Fe^{2+} + 2SO_4^{2-} + 2H^+ \quad \text{(R1)}$$

This process can be further stimulated by bioturbation and/or bioirrigation favouring the flushing of sulfate-rich water into deeper strata (Eq. (R1)) (Dantas et al., 2022; Lin et al., 2016; Zhao et al., 2021). The activity of benthic fauna, such as tubeworms, on the sediment redox conditions can involve the upper ~15 cm of sediment (Fischer et al., 2012), and the presence of pyritized tubes would support this hypothesis, which requires further investigations. The hydrate-bearing sediment core 367-GC shows extensive signs of bioturbation over half of its length down to ~38 cm bsf highlighted by recurrent tubeworm remnants.

To form non-evaporitic gypsum minerals in a diagenetic setting not only a sufficient amount of SO_4^{2-} but also Ca^{2+} ions are needed. As seawater in a normal marine environment contains ~10.55 mM of Ca^{2+} (Hoareau et al., 2011)(half of the amount of sulfate) and a significant oversaturation of the pore water has to be reached to favour the precipitation of calcium minerals like gypsum, additional processes providing Ca^{2+} to the pore waters have to be taken into account. One of the most likely processes to transport Ca^{2+} ions back into the pore water after deposition in a non-evaporitic environment is the dissolution of carbonates caused by pore water acidification. It has been proposed that the (re)oxidation of extensive amounts of pyrite can lead to a decreasing pH value in the pore waters due to the elevated production of H^+ ions (Eq. (R1))(Dantas et al., 2022; Lin et al., 2016; Zhao et al., 2021). In this study almost no to little amounts of carbonate were observed above 50 cm bsf as evidenced by especially low ln(Ca/Ti) values in the XRF and the lack of carbonate nodules even in the sedimentary intervals of the paleo SMTZ. Benthic and also planktonic foraminifera shells were completely missing in the interval directly above the modern SMTZ, from ~38 to 48 cm bsf, where also gypsum crystals were found. It also must be noted that findings of carbonate nodules and gypsum crystals in the investigated sediment core never coincide, which is consistent with the preference for gypsum formation occurring in a more acidic environment where carbonate formation/stability is not possible and, thus, more Ca^{2+} is available. These observations thus might point to an acidic sediment environment inducing carbonate dissolution. The recurring finding of authigenic gypsum at cold seeps associated with shallow gas hydrates (e.g. Kocherla, 2013; Lin et al., 2016; Zhang et al., 2018) suggests that hydrates play a critical role in its formation. Specifically, the process of hydrate formation generates an increase in pore water Ca^{2+} via ion exclusion: water and gas molecules are removed from pore water to form the clathrate structure while dissolved ions are excluded (Ussler and Paull, 1995). That process, in addition to the dissolution of carbonates induced by pyrite oxidation, further promotes the gypsum supersaturation and consequent precipitation. Previous studies also reported gypsum crystals in the shallow sediments of the HMMV (Milkov et al., 2004; Vogt et al., 1997), thus suggesting that gypsum formation might be widespread in this area. Therefore, HMMV represents an optimal natural laboratory to investigate the interplay between different processes on the gypsum biogeochemistry.

5.4. Gypsum as a proxy for decreasing methane fluxes

Geochemical proxies for methane oxidation are essential both in modern and ancient settings to reconstruct the history of seepage and biogeochemical processes in the sediment (e.g. Argentino et al., 2021; Chen et al., 2023; Hu et al., 2020; Yao et al., 2020). Among the authigenic minerals, gypsum has received growing attention as it appears to be more common at cold seeps than previously thought and plays a role in the sedimentary sulfur cycle (Lin et al., 2016; Liu et al., 2018; Pierre, 2017; Zhang et al., 2018; Zhao et al., 2021; Dantas et al., 2022). The reason why this mineral is not routinely applied as a proxy in seep studies might rely on the fact that it does not generally produce large accumulations detectable by common techniques such as XRF core scanning for barite fronts and methane-derived carbonates, as also shown in our study. Gypsum is commonly spotted and quantified via bulk sediment chemical and mineralogical analyses. In combination with other more established proxies (e.g., barite fronts, pyrite and methane-derived carbonates), the presence of gypsum in cold seeps can be clearly associated with paleo AOM and can be used to reconstruct SMTZ fluctuations through time with a higher stratigraphic resolution. Our results further consolidate the hypothesis that gypsum formation requires a combination of factors to form at cold seeps, such as a descending SMTZ (decreasing methane flux), a supply of SO_4^{2-} from pyrite oxidation and a source of calcium which can derive from carbonate dissolution and/or indirectly via gas hydrate formation. Consequently, gypsum formation is expected to be inhibited in settings marked by low iron availability for iron sulfide formation (and re-oxidation) (Formolo and Lyons, 2013) and carbonate-poor regions, which impose important limitations to its use as a proxy. However, owing to the recurrent association of seep-related gypsum and gas hydrates and the difficulty in identifying the occurrence of gas hydrates in the fossil record (Argentino et al., 2019; Bojanowski et al., 2015, 2021; Conti et al., 2021; Jakubowicz et al., 2015; Kennett and Fackler-Adams, 2000; Nelson et al., 2017), it is critical further explore seep-related gypsum biogeochemistry and its potential use as a proxy for paleo-gas hydrates. This can be done by using a multiproxy approach (Yao et al., 2020) based on the combination of geochemical, mineralogical and isotopic techniques. Furthermore, questions about the formation time and stability of gypsum as an authigenic mineral in the sediments of cold seep environments remain unanswered, and require further dedicated investigations.

6. Conclusions

Several authigenic minerals related to AOM were identified in a gas hydrate-bearing sediments collected from HMMV. The occurrence of authigenic carbonates, pyrites, and barite was identified by XRF enrichments in Ca, S, Fe and Ba,and confirmed by optical microscopy and SEM-EDS. Using previously published pore water data showing the position of the modern SMTZ at ~50 cm (Argentino et al., 2023), we were able to track the migration of the SMTZ through time and reconstruct the history of methane fluxes since at least 12.5 ka (the oldest paleo-SMTZ). Three paleo-SMTZ marked by pyrite and gypsum co-existence were found above the modern one at 7–10 cm, 13–18 cm and 19–21 cm, and match with carbonate-poor and foraminifera-free sediment intervals.

Our results provide evidence that the formation of gypsum as an authigenic mineral in the sediments of cold seep environments is closely linked to the distribution of pyrite previously produced by AOM and to the calcium accumulated in the pore waters by ion exclusion during gas hydrates formation. Consequently, gypsum formation is expected to be inhibited in settings marked by low iron availability for sulfide

formation and carbonate-poor settings. Decreasing methane fluxes are necessary for the re-oxidation of sulfides to dissolved sulfate in order to induce gypsum precipitation.

Although questions about the formation time and the stability of gypsum as an authigenic mineral in the sediments of cold seep environments remain unanswered, this study encourages further investigation to establish the use of gypsum as a potential additional proxy for decreasing methane fluxes in gas hydrate-bearing areas in modern and paleo settings.

CRediT authorship contribution statement

Cathrin Wittig: Writing – original draft, Visualization, Investigation, Formal analysis. **Claudio Argentino:** Writing – review & editing, Validation, Supervision, Methodology, Investigation, Data curation, Conceptualization. **Giuliana Panieri:** Writing – review & editing, Validation, Supervision, Project administration, Methodology, Funding acquisition, Conceptualization.

Declaration of competing interest

The authors declare the following financial interests/personal relationships which may be considered as potential competing interests: Giuliana Panieri reports financial support was provided by Norges Forskiningsrad. If there are other authors, they declare that they have no known competing financial interests or personal relationships that could have appeared to influence the work reported in this paper.

Data availability

All data have been presented in the main text.

Acknowledgments

The research was funded by the AKMA project (Norwegian Research Council grant No. 287869), and the Centre for Arctic Gas Hydrate, Environment and Climate (CAGE) (Norwegian Research Council grant No. 223259). The position of C.Argentino is covered by EMAN7 project (Norwegian Research Council grant No. 320100). We acknowledge chief scientists Kate Waghorn and Malin Waage, the captain and crew onboard R/V Helmer Hanssen for their assistance during the expedition CAGE20-3. We are grateful to the laboratory staff of the GeoLab (UiT) for support during core logging and analytical work. We thank three anonymous reviewers for their useful comments which improved the manuscript.

References

Argentino, C., Conti, S., Fioroni, C., Fontana, D., Sciences, G., Emilia, R., 2019. Evidences for paleo-gas hydrate occurrence: what we can infer for the Miocene of the northern apennines (Italy). Geosciences 9, 134. https://doi.org/10.3390/geosciences9030134.

Argentino, C., Savini, A., Panieri, G., 2022. Integrating fine-scale habitat mapping and pore water analysis: Implications and perspectives in cold seep research. In: Mienert, J., Berndt, C., Trehu, A., Camerlenghi, A., Liu, C.S. (Eds.), World Atlas of Submarine Gas Hydrates in Continental Margins. Springer, pp. 505–514. https://doi.org/10.1007/978-3-030-81186-0_43.

Argentino, C., Waghorn, K.A., Vadakkepuliyambatta, S., Polteau, S., Bünz, S., Panieri, G., 2021. Dynamic and history of methane seepage in the SW Barents Sea: new insights from leirdjupet fault complex. Sci. Rep. 11, 1–13. https://doi.org/10.1038/s41598-021-83542-0.

Argentino, C., Wittig, C., Peckmann, J., Panieri, G., 2023. Nitrogen uptake by methanotrophic consortia in deep-water gas hydrate-bearing sediments. Chem. Geol. 636, 121638 https://doi.org/10.1016/j.chemgeo.2023.121638.

Bazzaro, M., Ogrinc, N., Relitti, F., Lucchi, R.G., Giani, M., Adami, G., Pavoni, E., De Vittor, C., 2020. Geochemical signatures of intense episodic anaerobic oxidation of methane in near-surface sediments of a recently discovered cold seep (Kveithola trough, NW Barents Sea). Mar. Geol. 425, 106189 https://doi.org/10.1016/j.margeo.2020.106189.

Berndt, C., Planke, S., Mienert, J., Bünz, S., Eriksen, F., 2006. The plumbing system of the Håkon mosby Mud Volcano – new insights from high-resolution 3D seismic data. In: AAPG/GSTT HEDBERG CONFERENCE, vol. 4.

Boetius, A., Wenzhöfer, F., 2013. Seafloor oxygen consumption fuelled by methane from cold seeps. Nat. Geosci. 6, 725–734. https://doi.org/10.1038/ngeo1926.

Bohrmann, G and Torres, ME (2016) Marine Gas Hydrates. In: Harff, J, Meschede, M, Petersen, S and Thiede, J (eds.) Encyclopedia of Marine Geosciences. Encyclopedia of Earth Sciences Series. Springer Netherlands, 433-437. doi:10.1007/978-94-007-6644-0_168-2.

Bojanowski, M.J., Bagiński, B., Guillermier, C., Franchi, I.A., 2015. Carbon and oxygen isotope analysis of hydrate-associated Oligocene authigenic carbonates using NanoSIMS and IRMS. Chem. Geol. 416, 51–64. https://doi.org/10.1016/j.chemgeo.2015.10.021.

Bojanowski, M.J., Oszczypko-Clowes, M., Barski, M., Oszczypko, N., Radzikowska, M., Ciesielska, Z., 2021. Slope destabilization provoked by dissociation of gas hydrates in the Outer Carpathian basin during the Oligocene: sedimentological, petrographic, isotopic and biostratigraphic record. Mar. Petrol. Geol. 123, 104585 https://doi.org/10.1016/j.marpetgeo.2020.104585.

Bünz, S., Panieri, G., 2022. CAGE21-1 cruise report: AKMA-AKER-GReAT. CAGE – cent. Arct. Gas hydrate. Environ. Clim. Rep. Ser. 9 https://doi.org/10.7557/cage.6677.

Carter, S.C., Paytan, A., Griffith, E.M., 2020. Toward an improved understanding of the marine barium cycle and the application of marine barite as a paleoproductivity proxy. Minerals 10, 1–24. https://doi.org/10.3390/min10050421.

Chen, Q., Hu, Y., Peckmann, J., Chen, L., Feng, D., Liang, Q., Chen, D., 2023. The formation of authigenic phosphorus minerals in cold-seep sediments from the South China Sea: implications for carbon cycling below the sulfate-methane transition. Mar. Petrol. Geol. 155, 106425.

Conti, S., Argentino, C., Fioroni, C., Salocchi, A.C., Fontana, D., 2021. Miocene seep-carbonates of the northern apennines (Emilia to umbria, Italy): an overview. Geosci. 11 https://doi.org/10.3390/geosciences11020053.

Dantas, R.C., Hassan, M.B., Cruz, F.W., Jovane, L., 2022. Evidence for methane seepage in South Atlantic from the occurrence of authigenic gypsum and framboidal pyrite in deep-sea sediments. Mar. Petrol. Geol. 142, 105727 https://doi.org/10.1016/j.marpetgeo.2022.105727.

Fallati, L., Panieri, G., 2023. Microbathymetry of Haakon Mosby mud volcano, acquired with multibeam echosounder mounted on ROV ÆGIR6000, during the CAGE21-1 cruise within the AKMA project. DataverseNO V2. https://doi.org/10.18710/C1R1IN.

Fallati, L., Panieri, G., Argentino, C., Varzi, A.G., Bünz, S., Savini, A., 2023. Characterizing Håkon Mosby Mud Volcano (Barents Sea) cold seep systems by combining ROV-based acoustic data and underwater photogrammetry. Frontiers in Marine Science 10, 1269197.

Faust, J.C., Stevenson, M.A., Abbott, G.D., Knies, J., Tessin, A., Mannion, I., Ford, A., Hilton, R., Peakall, J., März, C., 2020. Does Arctic warming reduce preservation of organic matter in Barents Sea sediments?: Barents Sea surface sediment composition. Philos. Trans. R. Soc. A Math. Phys. Eng. Sci. 378, 20190364 https://doi.org/10.1098/rsta.2019.0364.

Feseker, T., Foucher, J.P., Harmegnies, F., 2008. Fluid flow or mud eruptions? Sediment temperature distributions on Håkon Mosby mud volcano, SW Barents Sea slope. Mar. Geol. 247, 194–207. https://doi.org/10.1016/j.margeo.2007.09.005.

Feseker, T., Boetius, A., Wenzhöfer, F., Blandin, J., Olu, K., Yoerger, D.R., Camilli, R., German, C.R., De Beer, D., 2014. Eruption of a deep-sea mud volcano triggers rapid sediment movement. Nat. Commun. 5, 1–8. https://doi.org/10.1038/ncomms6385.

Fischer, D., Sahling, H., Nöthen, K., Bohrmann, G., Zabel, M., Kasten, S., 2012. Interaction between hydrocarbon seepage, chemosynthetic communities, and bottom water redox at cold seeps of the Makran accretionary prism: insights from habitat-specific pore water sampling and modeling. Biogeosciences 9, 2013–2031. https://doi.org/10.5194/bg-9-2013-2012.

Formolo, M.J., Lyons, T.W., 2013. Sulfur biogeochemistry of cold seeps in the Green Canyon region of the Gulf of Mexico. Geochem. Cosmochim. Acta 119, 264–285. https://doi.org/10.1016/j.gca.2013.05.017.

Foucher, J.P., Westbrook, G.K., Boetius, A., Ceramicola, S., Dupré, S., Mascle, J., Mienert, J., Pfannkuche, O., Pierre, C., Praeg, D., 2009. Structure and drivers of cold seep ecosystems. Oceanography 22, 92–109. https://doi.org/10.5670/oceanog.2009.11.

Foucher, J.P., Dupré, S., Scalabrin, C., Feseker, T., Harmegnies, F., Nouzé, H., 2010. Changes in seabed morphology, mud temperature and free gas venting at the Håkon Mosby mud volcano, offshore northern Norway, over the time period 2003-2006. Geo Mar. Lett. 30, 157–167. https://doi.org/10.1007/s00367-010-0193-z.

Gong, S., Luo, M., Griffith, E.M., Peckmann, J., Liang, Q., Feng, D., 2023. Calcium isotopic fractionation during aragonite and high-Mg calcite precipitation at methane seeps. Earth Planet Sci. Lett. 622, 118419.

Himmler, T., Sahy, D., Martma, T., Bohrmann, G., Plaza-Faverola, A., Bünz, S., Condon, D.J., Knies, J., Lepland, A., 2019. A 160,000-year-old history of tectonically controlled methane seepage in the Arctic. Sci. Adv. 5 https://doi.org/10.1126/sciadv.aaw1450.

Hjelstuen, B.O., Eldholm, O., Faleide, J.I., Vogt, P.R., 1999. Regional setting of hakon mosby Mud Volcano, SW Barents Sea margin. Geo Mar. Lett. 19, 22–28. https://doi.org/10.1007/s003670050089.

Hoareau, G., Monnin, C., Odonne, F., 2011. The stability of gypsum in marine sediments using the entire ODP/IODP pore water composition database. Mar. Geol. 279, 87–97. https://doi.org/10.1016/J.MARGEO.2010.10.014.

Hong, W.L., Latour, P., Sauer, S., Sen, A., Gilhooly, W.P., Lepland, A., Fouskas, F., 2020. Iron cycling in Arctic methane seeps. Geo Mar. Lett. 40, 391–401. https://doi.org/10.1007/s00367-020-00649-5.

Hu, Y., Feng, D., Peckmann, J., Gong, S.G., Liang, Q.Y., Wang, H.B., Chen, D.F., 2020. The impact of diffusive transport of methane on pore-water and sediment geochemistry constrained by authigenic enrichments of carbon, sulfur, and trace elements: a case study from the Shenhu area of the South China Sea. Chem. Geol. 553, 119805.

Jakubowicz, M., Dopieralska, J., Belka, Z., 2015. Tracing the composition and origin of fluids at an ancient hydrocarbon seep (Hollard Mound, Middle Devonian, Morocco): a Nd, REE and stable isotope study. Geochem. Cosmochim. Acta 156, 50–74. https://doi.org/10.1016/j.gca.2015.02.027.

Jerosch, K., Schlüter, M., Foucher, J.P., Allais, A.G., Klages, M., Edy, C., 2007. Spatial distribution of mud flows, chemoautotrophic communities, and biogeochemical habitats at Håkon Mosby Mud Volcano. Mar. Geol. 243, 1–17. https://doi.org/10.1016/j.margeo.2007.03.010.

Johnson, J.E., Phillips, S.C., Clyde, W.C., Giosan, L., Torres, M.E., 2021. Isolating detrital and diagenetic signals in magnetic susceptibility records from methane-bearing marine sediments. G-cubed 22, 1–21. https://doi.org/10.1029/2021GC009867.

Jørgensen, B.B., 2021. Sulfur biogeochemical cycle of marine sediments. Geochemical Perspect 145–307. https://doi.org/10.7185/geochempersp.10.2.

Kennett, J.P., Fackler-Adams, B.N., 2000. Relationship of clathrate instability to sediment deformation in the upper Neogene of California. Geology 28, 215–218. https://doi.org/10.1130/0091-7613(2000)28<215:ROCITS>2.0.CO.

Kocherla, M., 2013. Authigenic gypsum in gas-hydrate associated sediments from the East coast of India (bay of bengal). Acta Geol. Sin. - English 87, 749–760. https://doi.org/10.1111/1755-6724.12086.

Kopittke, P.M., Menzies, N., Fulton, I.M., 2004. Gypsum solubility in seawater, and its application to bauxite residue amelioration. Aust. J. Soil Res. 42, 953–960.

Kravchishina, M.D., Lein, A.Y., Flint, M.V., Baranov, B.V., Miroshnikov, A.Y., Dubinina, E.O., Dara, O.M., Boev, A.G., Savvichev, A.S., 2021. Methane-derived authigenic carbonates on the seafloor of the laptev sea shelf. Front. Mar. Sci. 8 https://doi.org/10.3389/fmars.2021.690304.

Levitan, M.A., Lavrushin, Y.A., 2009. In: Sedimentation History in the Arctic Ocean and Subarctic Seas for the Last 130 Kyr, Lecture Notes in Earth Sciences. Springer, Berlin Heidelberg, Berlin, Heidelberg. https://doi.org/10.1007/978-3-642-00288-5.

Lin, Q., Wang, J., Algeo, T.J., Su, P., Hu, G., 2016. Formation mechanism of authigenic gypsum in marine methane hydrate settings: evidence from the northern South China Sea. Deep. Res. Part I Oceanogr. Res. Pap. 115, 210–220. https://doi.org/10.1016/j.dsr.2016.06.010.

Liu, X., Li, A., Dong, J., Zhuang, G., Xu, F., Wan, S., 2018. Non-evaporative origin for gypsum in mud sediments from the East China Sea shelf. Mar. Chem. 205, 90–97. https://doi.org/10.1016/j.marchem.2018.08.009.

Lösekann, T., Knittel, K., Nadalig, T., Fuchs, B., Niemann, H., Boetius, A., Amann, R., 2007. Diversity and abundance of aerobic and anaerobic methane oxidizers at the haakon mosby Mud Volcano, Barents Sea. Appl. Environ. Microbiol. 73, 3348–3362. https://doi.org/10.1128/AEM.00016-07.

Milkov, A.V., Vogt, P.R., Crane, K., Lein, A.Y., Sassen, R., Cherkashev, G.A., 2004. Geological, geochemical, and microbial processes at the hydrate-bearing Håkon Mosby mud volcano: a review. Chem. Geol. 205, 347–366. https://doi.org/10.1016/j.chemgeo.2003.12.030.

Nelson, C.S., Nyman, S.L., Campbell, K.A., Rowland, J.R., Nyman, S.L., Campbell, K.A., Influence, J.R.R., 2017. Influence of faulting on the distribution and development of cold seep-related dolomitic conduit concretions at East Cape. New Zealand 8306. https://doi.org/10.1080/00288306.2017.1372489.

Niemann, H., Lösekann, T., De Beer, D., Elvert, M., Nadalig, T., Knittel, K., Amann, R., Sauter, E.J., Schlüter, M., Klages, M., Foucher, J.-P., Boetius, A., 2006. Novel microbial communities of the Haakon Mosby mudvolcano and their role as a methanesink. Nature 443, 854–858.

Panieri, G., Bünz, S., Fornari, D.J., Escartin, J., Serov, P., Jansson, P., Torres, M.E., Johnson, J.E., Hong, W., Sauer, S., Garcia, R., 2017. An integrated view of the methane system in the pockmarks at Vestnesa Ridge, 79 N. Mar. Geol. 390, 282–300. https://doi.org/10.1016/j.margeo.2017.06.006.

Pape, T., Feseker, T., Kasten, S.Fischer, Bohrmann, D., 2011. Distribution and abundance of gas hydrates in near-surface deposits of the Håkon mosby Mud Volcano, SW Barents Sea. G-cubed 12. https://doi.org/10.1029/2011GC003575.

Perez-Garcia, C., Feseker, T., Mienert, J., Berndt, C., 2009. The Håkon Mosby mud volcano: 330 000 years of focused fluid flow activity at the SW Barents Sea slope. Mar. Geol. 262, 105–115. https://doi.org/10.1016/j.margeo.2009.03.022.

Pierre, C., 2017. Origin of the authigenic gypsum and pyrite from active methane seeps of the southwest African Margin. Chem. Geol. 449, 158–164. https://doi.org/10.1016/j.chemgeo.2016.11.005.

Pirlet, H., Wehrmann, L.M., Foubert, A., Brunner, B., Blamart, D., De Mol, L., Van Rooij, D., Dewanckele, J., Cnudde, V., Swennen, R., Duyck, P., Henriet, J., 2012. Unique authigenic mineral assemblages reveal different diagenetic histories in two neighbouring cold-water coral mounds on Pen Duick Escarpment, Gulf of Cadiz. Sedimentology 59, 578–604. https://doi.org/10.1111/j.1365-3091.2011.01267.

Reeburgh, W.S., 2007. Oceanic methane Biogeochemistry. Chem. Rev. 107, 486 – 513. https://doi.org/10.1021/cr050362v.

Riedinger, N., Kasten, S., Gröger, J., Franke, C., Pfeifer, K., 2006. Active and buried authigenic barite fronts in sediments from the Eastern Cape Basin. Earth Planet Sci. Lett. 241, 876–887. https://doi.org/10.1016/j.epsl.2005.10.032.

Ruban, A., Rudmin, M., Dudarev, O., Mazurov, A., 2020. The formation of authigenic carbonates at a methane seep site in the northern part of the Laptev sea. Minerals 10, 1–14. https://doi.org/10.3390/min10110948.

Schippers, A., Jorgensen, B.B., 2002. Biogeochemistry of pyrite and iron sulfide oxidation in marine sediments. Geochem. Cosmochim. Acta 66, 85–92. https://doi.org/10.1016/S0016-7037(01)00745-1.

Suess, E., 2020. Marine cold seeps: background and recent advances. In: Wilkes, H. (Ed.), Hydrocarbons, Oils and Lipids: Diversity, Origin, Chemistry and Fate. Springer Nature Switzerland AG, pp. 747–767. https://doi.org/10.1007/978-3-319-90569-3.

Sun, T., Cao, K., Yin, P., Jiang, X., Tian, Y., 2023. Authigenic pyrite and gypsum minerals in offshore Zhoushan sediments: morphology, formation, and environmental implications. Front. Earth Sci. 11 https://doi.org/10.3389/feart.2023.1165809Torres.

Ussler, W., Paull, C.K., 1995. Effects of ion exclusion and isotopic fractionation on pore water geochemistry during gas hydrate formation and decomposition. Geo-Marine Letters 15, 37–44. https://doi.org/10.1007/BF01204496.

Vanneste, H., James, R.H., Kelly-Gerreyn, B.A., Mills, R.A., 2013. Authigenic barite records of methane seepage at the carlos ribeiro mud volcano (gulf of cadiz). Chem. Geol. 354, 42–54. https://doi.org/10.1016/j.chemgeo.2013.06.010.

Vogt, P.R., Cherkashev, G., Ginsburg, G., Ivanov, G., Milkov, A., Crane, K., Lein, A., Sundvor, E., Pimenov, N., Egorov, A., 1997. Haakon mosby mud volcano provides unusual example of venting. Eos 78, 549–557. https://doi.org/10.1029/97eo00326.

Waghorn, K.A., Malin, W., Argentino, C., 2020. CAGE20-3 cruise report: geochemical and sedimentological investigation into ingøydjupet, Håkon mosby Mud Volcano and the sorvestnaget sand waves. CAGE–Centre for Arctic Gas Hydrate, Environment and Climate Report Series 8. https://doi.org/10.7557/cage.6913.

Wallmann, K., Schicks, J.M., 2020. Gas hydrates as an unconventional hydrocarbon source. In: Wilkes, H. (Ed.), Hydrocarbons, Oils and Lipids: Diversity, Origin, Chemistry and Fate. Springer Nature Switzerland AG, pp. 651–666. https://doi.org/10.1007/978-3-319-90569-3.

Whiticar, M.J., 2020. The biogeochemical methane cycle. In: Wilkes, H. (Ed.), Hydrocarbons, Oils and Lipids: Diversity, Origin, Chemistry and Fate. Springer Nature Switzerland AG, pp. 669–746. https://doi.org/10.1007/978-3-319-90569-3.

Whiticar, M.J., Faber, E., 1986. Methane oxidation in sediment and water column environments-isotope evidence. Org. Geochem. 10, 759–768.

Yao, H., Niemann, H., Panieri, G., 2020. Multi-proxy approach to unravel methane emission history of an Arctic cold seep. Quat. Sci. Rev. 244, 106490 https://doi.org/10.1016/j.quascirev.2020.106490.

Zhang, M., Lu, H., Guan, H., Liu, L., Wu, D., Wu, N., 2018. Methane seepage intensities traced by sulfur isotopes of pyrite and gypsum in sediment from the Shenhu area, South China Sea. Acta Oceanologica Sinica 37, 20–27.

Zhao, J., Wang, J., Phillips, S.C., Liang, J., Su, P., Lin, Q., Chen, C., Liu, J., 2021. Non-evaporitic gypsum formed in marine sediments due to sulfate-methane transition zone fluctuations and mass transport deposits in the northern South China Sea. Mar. Chem. 233, 103988 https://doi.org/10.1016/j.marchem.2021.103988.

Zhou, Y., Di, P., Li, N., Chen, F., Su, X., Zhang, J., 2020. Unique authigenic mineral assemblages and planktonic foraminifera reveal dynamic cold seepage in the southern South China sea. Minerals 10, 275. https://doi.org/10.3390/min10030275.